JACS Au
AN OPEN ACCESS JOURNAL OF THE AMERICAN CHEMICAL SOCIETY

pubs.acs.org/jacsau
Article

Decoupling Electrolytic Water Splitting by an Oxygen-Mediating Process

Mingze Xu,[#] Jianying Wang,[#] Shi-Gang Sun, and Zuofeng Chen*

Cite This: JACS Au 2024, 4, 3964−3975

Read Online

ACCESS | Metrics & More | Article Recommendations | Supporting Information

ABSTRACT: Decoupled water electrolysis systems, incorporating a reversible redox mediator that allows for the construction of membrane-free electrolyzers, have emerged as a promising approach to produce high-purity hydrogen with remarkable flexibility. The key factor crucial for practical applications lies in the development of mediator electrodes that possess suitable redox potential, high redox capacity, excellent cycling reversibility and stability. Herein, we introduce a novel concept of oxygen-mediating redox mediators (ORMs) employing Bi_2O_3 as an example material, which are capable of sequestering oxygen during the hydrogen evolution reaction and subsequently releasing it to generate oxygen gas under alkaline conditions. Thanks to its remarkable reversible redox activity and specific capacity, the Bi_2O_3 electrode boasts an impressive reversible specific capacity of 300.8 mA h g^{-1} and delivers outstanding cycling performance for >1000 cycles at a current density of 2.0 A g^{-1}. Furthermore, the implementation of such a decoupled alkaline water electrolysis system can be integrated with a Bi_2O_3−Zn battery, enabling both power-to-fuel (hydrogen production) and chemical-to-power (rechargeable Bi_2O_3−Zn battery) conversion. With many oxygen-carrier materials readily available and the potential integration with rechargeable alkaline batteries, this study provides an alternative competitive route for membrane-free decoupled water splitting through the oxygen-mediating mechanism with combined energy transformation and storage.

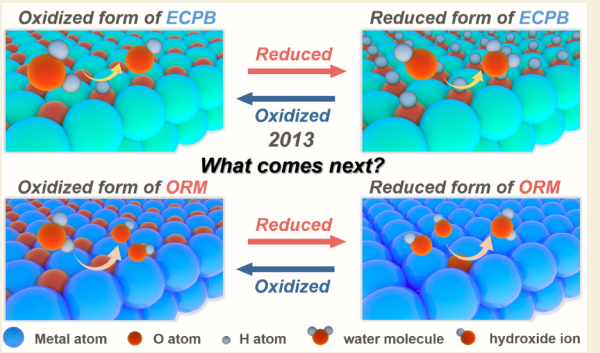

KEYWORDS: *oxygen-mediating redox mediators, decoupled water electrolysis, membrane-free cell, bismuth oxide, Bi_2O_3−Zn battery*

INTRODUCTION

Hydrogen has long been considered an ideal energy candidate after the oil-crises of the mid-1970s due to its high energy density and environmentally friendly product (H_2O).[1−3] Among the various methods for hydrogen production, water electrocatalysis driven by renewable energy sources is widely regarded as one of the most attractive and sustainable approaches.[4−7] In conventional water electrolysis systems (Scheme 1a), the cathodic hydrogen evolution reaction (HER) is accompanied by the generation of oxygen gas through the oxygen evolution reaction (OER) at the anode, which causes several non-negligible issues. First, the introduction of an ion-exchange membrane to segregate the concurrently generated H_2 and O_2 gases results in a substantial increase in energy consumption due to mass transfer resistance.[8−13] Second, the generated O_2 gas may cross the membrane and mix with H_2 gas due to the unbalanced pressure between the two chambers, creating an explosive H_2/O_2 mixture.[14] Additionally, the formation of reactive oxygen species (ROS) would exacerbate membrane degradation, consequently diminishing its lifespan and escalating the cost of electrolyzers.[10] To overcome these drawbacks, the decoupled water splitting strategy was proposed first by Cronin's group in 2013.[15] By this strategy, the electrons and protons generated during the OER are reversibly stored in the redox mediator, also known as electron-coupled proton buffer (ECPB), rather than directly producing H_2. Subsequent reoxidation of the redox mediator releases these protons and electrons for H_2 production.

This pioneering research undeniably presented an insightful pattern for future water electrolysis technology. Over the past decade, a range of redox mediators have been explored to achieve a decoupling strategy for acidic, alkaline, or neutral water electrolysis. These reported mediators can be categorized into two main types: liquid redox mediators (LRMs, like $H_3PMo_{12}O_{40}$,[15,16] $H_4SiW_{12}O_{40}$,[17] 1,4-hydroquinone,[18] anthraquinone-2,7-disulfonic acid,[19] etc.) and solid-state redox mediators (SRMs, like $Ni(OH)_2$,[20−22] PTPAn,[23] PANI,[24] PTO,[25] etc.), as shown in Figure S1. The majority of these

Received: August 6, 2024
Revised: September 2, 2024
Accepted: September 3, 2024
Published: September 19, 2024

Scheme 1. Schematic Diagrams of the Reaction Process for (a) Conventional Alkaline Water Electrolysis, (b) Decoupled Alkaline Water Electrolysis Based on the ECPB, Where *N* Represents the ECPB in the Oxidized Form (e.g., NiOOH[20] and MnO_2[39]) and *NH* Represents the ECPB in the Reduced and Protonated Form (e.g., $Ni(OH)_2$[20] and MnOOH[39]) and (c) Decoupled Alkaline Water Electrolysis Using Bi_2O_3/Bi^0 Redox Mediator; (d) CV Curve of the Bi_2O_3 Electrode (Blue line), and LSV Curves of the Commercial RuO_2/IrO_2-Coated and Pt-Coated Ti-Mesh Electrodes for the OER (Orange Line) and the HER (Cyan Line) in 1 M KOH at a Scan Rate of 0.1 mV s^{-1}.

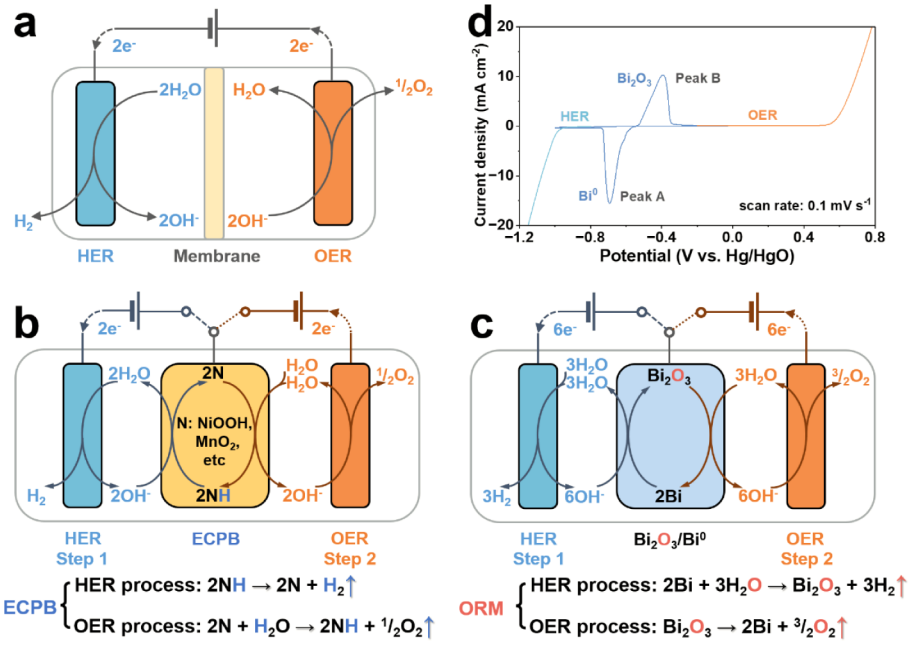

mediators fulfill the roles of ECPBs, which exhibit the capacity to function as reversible electron and proton donors/acceptors with redox potentials lying energetically between the HER and OER (Scheme 1b).[15] As evidenced by the existing literature, a number of redox mediators have been applied in the decoupled water splitting strategy in acidic solutions, surpassing their utilization in alkaline media.[11,14,20−30] Compared to acidic water electrolysis, alkaline water electrolysis is inherently low-cost due to the use of nonprecious catalysts.[31,32] As of the present, $Ni(OH)_2$ remains among the scarce solid-state redox mediators capable of adhering to the ECPB concept for decoupling water electrolysis in alkaline media (Figures S2 and S3).[20−22] To expand the applicability of the decoupling strategy, it is crucial to uncover new mediating mechanisms to facilitate the search for suitable redox mediators, especially under alkaline conditions.

In light of this background, our primary focus centers on the feasibility of initially sequestering oxygen within a redox mediator during the reduction of water to H_2 and subsequently liberating it to produce O_2 under alkaline conditions. This decoupling scheme is distinctly different from the aforementioned ECPBs strategy (hydrogen-mediating redox mediator), which we called the ORMs strategy (oxygen-mediating redox mediators). Whereas, the oxygen-mediating processes have been recognized in the fields of solid oxide fuel cell (SOFC, Figure S4),[33] solid oxide electrolytic cell (SOEC, Figure S5),[34] and chemical looping process (Figure S6),[35] there is no relevant report on the oxygen-mediating water electrolysis decoupling. Recent years have seen substantial advances in the design, formulation, and manufacture of these oxygen carrier materials and their incorporation into the energy configurations and chemical looping reactors for the energy transformation and various chemicals production. Building upon this premise, suitable ORMs are the key for the development of oxygen-mediating water electrolysis decoupling systems in alkaline media.

Drawing upon the aforementioned ORMs mechanism, a varied array of cost-effective and alkaline-stable battery-type metal oxide materials can be considered as potential candidates for ORMs in decoupled alkaline water splitting. Normally, the employed redox mediators are required to possess suitable redox potential, high charge storage capability, as well as excellent cycling reversibility and stability. Given this, Bi_2O_3 stands out among those oxygen carrier materials due to its exceptional reversible redox activity ($Bi_2O_3 \leftrightarrow Bi^0$), high theoretical specific capacity quantified at 345.11 mA h g^{-1}, and good recycling stability, which has prompted its investigation and application within the realm of energy storage.[36−38] The conversion process between Bi_2O_3 and Bi^0 can be effectuated via the transfer of oxygen under alkaline conditions, which is akin to the ORMs mechanism and thus exhibits an application prospect for the decoupled alkaline water splitting.

In this study, employing Bi_2O_3/Bi^0 as an ORM that is distinct from earlier proposed ECPBs, we effectively decoupled the processes of the HER and OER temporally and spatially in alkaline media. In this configuration, H_2 production by the cathodic reduction of water is contingent upon the anodic oxidation of Bi^0 ($Bi^0 \rightarrow Bi_2O_3$), while the subsequent O_2 generation involves the anodic oxidation of OH^- and the cathodic reduction of Bi_2O_3 ($Bi_2O_3 \rightarrow Bi^0$), as shown in Scheme 1c. The Bi_2O_3 boasts an impressive reversible specific capacity of up to 300.8 mA h g^{-1} and delivers outstanding cycling performance, with 87.8% capacity retention after 1000 cycles at a current density of 2.0 A g^{-1}. Additionally, the Bi_2O_3 electrode can couple with a zinc anode to create a Bi_2O_3−Zn battery, achieving energy transformation and storage through

https://doi.org/10.1021/jacsau.4c00710
JACS Au 2024, 4, 3964−3975

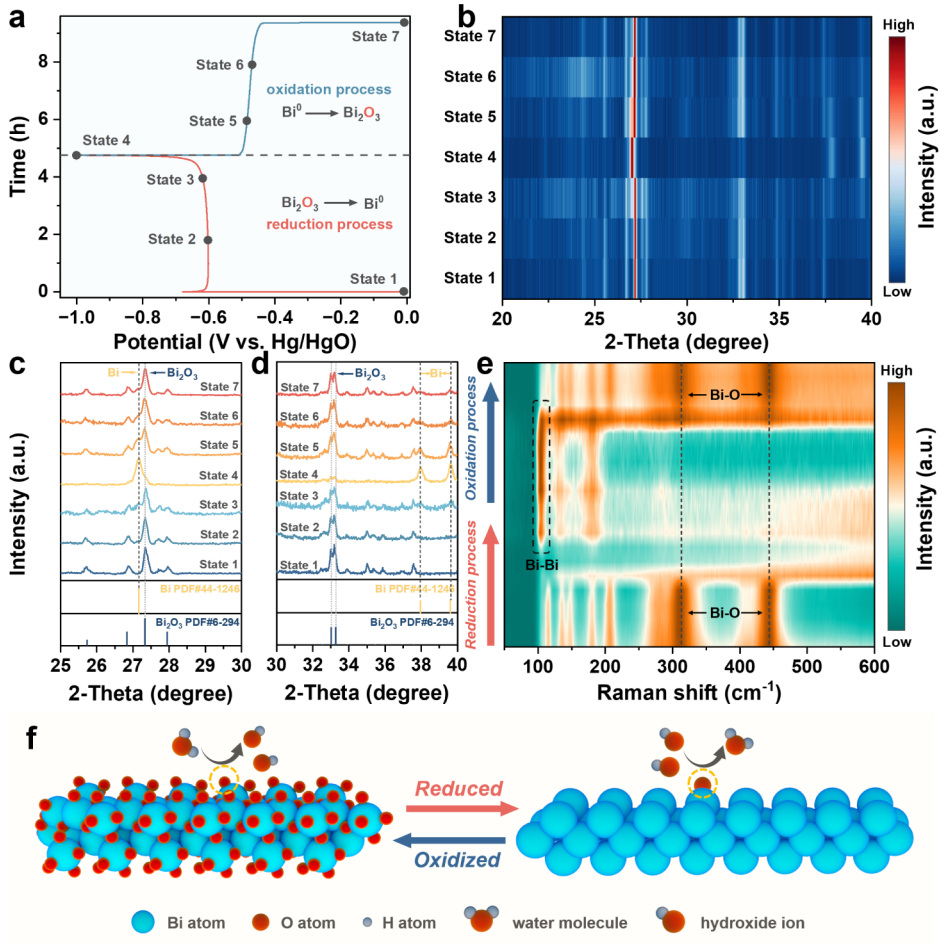

Figure 1. Redox mechanism of Bi_2O_3 in an alkaline electrolyte. (a) GCD test at 5 mA (the first charge/discharge curves). (b–d) *Quasi-in situ* XRD patterns at selected states of the GCD test. (e) *In situ* Raman patterns of the Bi_2O_3 electrode at different potentials. (f) Schematic diagram of the redox conversion between Bi_2O_3 and Bi^0 in an alkaline electrolyte.

Bi^0–Bi_2O_3 interconversion. By integration of this Bi_2O_3–Zn battery with the ORMs strategy, it enables the production of H_2 through the decoupled water electrolysis and the subsequent regeneration of Bi^0 through the discharge of the Bi_2O_3–Zn battery with concomitant energy output. This intrigue electrolysis-battery integrated configuration may lead to more convenient and competitive routes for the hydrogen production with combined energy transformation and storage.

RESULTS AND DISCUSSION

Redox Behaviors and Reaction Mechanism of the Bi_2O_3 Electrode

In this study, the synthesis of Bi_2O_3 was achieved through a hydrothermal reaction followed by annealing in an ambient air atmosphere. The crystalline composition (α-Bi_2O_3 phase) and morphological features (walnut-like) of the as-synthesized Bi_2O_3 were meticulously characterized using X-ray diffraction (XRD) and scanning electron microscopy (SEM) techniques, as shown in Figure S7. Prior to the assembly of the decoupled water splitting device, an extensive examination of the redox characteristics of the Bi_2O_3 mediator was conducted in an alkaline electrolyte using a three-electrode setup. As illustrated in Scheme 1d, the distinct redox peaks in cyclic voltammogram (CV) curve are prominently discernible at −0.69 V and −0.39 V (vs Hg/HgO), attributed to the reversible cycling between Bi_2O_3 and Bi^0, a phenomenon that will be expounded upon in subsequent discussions. Furthermore, linear sweep voltammogram (LSV) curves for the OER and HER were acquired utilizing commercially available RuO_2/IrO_2-coated and Pt-coated Ti-mesh electrodes, respectively (Scheme 1d). Notably, the typical potential window associated with the Bi_2O_3/Bi^0 redox couple is positioned between the onset potential for the OER and HER. This outcome substantiates the feasibility of employing Bi_2O_3/Bi^0 as a solid-state redox mediator to decouple the conventional alkaline water electrolysis process into two distinct stages.

To investigate the mediating mechanism of Bi_2O_3 for decoupling water splitting, it is imperative to unravel the intricate redox mechanism underlying Bi_2O_3/Bi^0. First, we conducted a comprehensive examination on the phase transition and the resultant product composition via the *quasi-in situ* XRD technique. Figure 1a–d illustrate the galvanostatic charge–discharge (GCD) profiles of the Bi_2O_3 electrode at a current density of 5 mA and the corresponding XRD patterns collected at various charge–discharge states, respectively. In Figure 1b, it is discernible that the diffraction peaks associated with Bi_2O_3, situated at 27.3° (120), 33.0° (−121) and 33.3° (200), undergo conspicuous alterations in peak intensity during the charge/discharge process, concomitant with the emergence and disappearance of new peaks. Upon closer examination of the enlarged XRD patterns in

https://doi.org/10.1021/jacsau.4c00710
JACS Au 2024, 4, 3964–3975

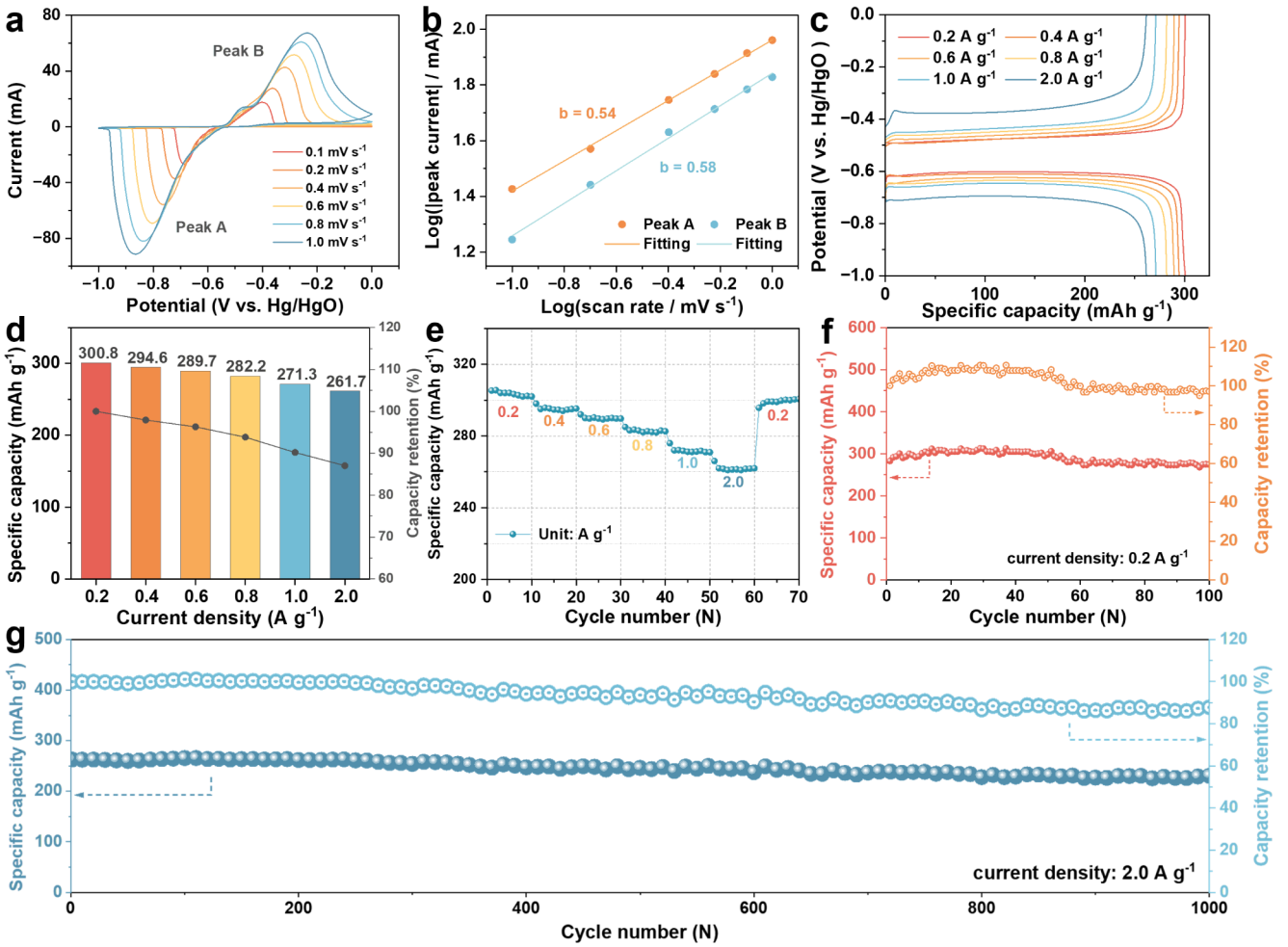

Figure 2. Electrochemical performance of Bi_2O_3 in an alkaline electrolyte. (a) CV curves at different scan rates. (b) Relationship between the log (peak current) and log (scan rate). (c) GCD curves and (d) corresponding specific capacity at different current densities. (e) Rate performance of the Bi_2O_3 electrode. Cycling performances at (f) 0.2 A g^{-1} and (g) 2.0 A g^{-1}.

Figure 1c,d (full XRD patterns in Figure S8), it becomes evident that, as the Bi_2O_3 electrode undergoes reduction from State 1 to State 4, a series of diffraction peaks appear at 27.2° (012), 37.9° (104) and 39.6° (110), indicative of the presence of Bi^0 (PDF#44-1246). The oxidative transition from State 4 to State 7 is characterized by a diminishment in the diffraction peaks of Bi^0, concomitant with the reappearance of diffraction peaks associated with Bi_2O_3 (PDF#6-294). To gain further insight into the oxygen-mediated properties of the Bi_2O_3 electrode, we conducted *in situ* Raman spectroscopy measurements. As delineated in Figures 1e and S9, two typical Raman peaks at 313 and 443 cm^{-1} are ascribed to Bi−O stretching vibrations of Bi_2O_3 in the initial state.[40,41] During the reduction process, the intensity of the Bi−O stretching vibration gradually weakens while the Bi−Bi stretching vibration becomes apparent.[42,43] On the other hand, as the electrode enters the oxidation stage, the Bi−Bi stretching vibration progressively diminishes accompanied by the reappearance of the Bi−O stretching vibration. Both the *quasi-in situ* XRD and *in situ* Raman data provide compelling evidence of a highly reversible redox reaction transpiring between Bi_2O_3 and Bi^0.

To ascertain the occurrence of lattice oxygen storage or release during the redox process of Bi_2O_3/Bi, a comprehensive investigation encompassing elemental content analysis and morphological observations was conducted at various charge/discharge states. As illustrated in Figures S10−12, the observed morphological changes align well with the interconversion between the monoclinic crystal structure of Bi^0 and the monoclinic crystal structure of Bi_2O_3, as evidenced by the *quasi-in situ* XRD patterns in Figure 1b−d. Based on the map sum spectra presented in Figures S11 and S12, the atomic ratio of Bi/O at each state was calculated and visually depicted in Figure S13 and Table S1. Accordingly, the redox mechanism of the Bi_2O_3 electrode in an alkaline electrolyte is summarized in Figure 1f, with the reaction equations elaborated below:

$$\text{Reduction process: } BI_2O_3 + 3H_2O + 6e^- \rightarrow 2Bi + 6OH^- \quad (1)$$

$$\text{Oxidation process: } 2Bi + 6OH^- - 6e^- \rightarrow Bi_2O_3 + 3H_2O \quad (2)$$

The redox reactions described above signify reversible conversion between Bi_2O_3 and Bi^0, in accordance with the ORM mechanism. Consequently, the utilization of Bi_2O_3 as an ORM for the construction of a decoupled alkaline water electrolysis system is entirely feasible. As illustrated in Scheme 1c, the comprehensive operational mechanism can be succinctly summarized as follows:

During the O_2 production process:

$$\text{Anode: } 6OH^- \rightarrow 3H_2O + 6e^- + 3/2O_2 \quad (3)$$

https://doi.org/10.1021/jacsau.4c00710
JACS Au 2024, 4, 3964−3975

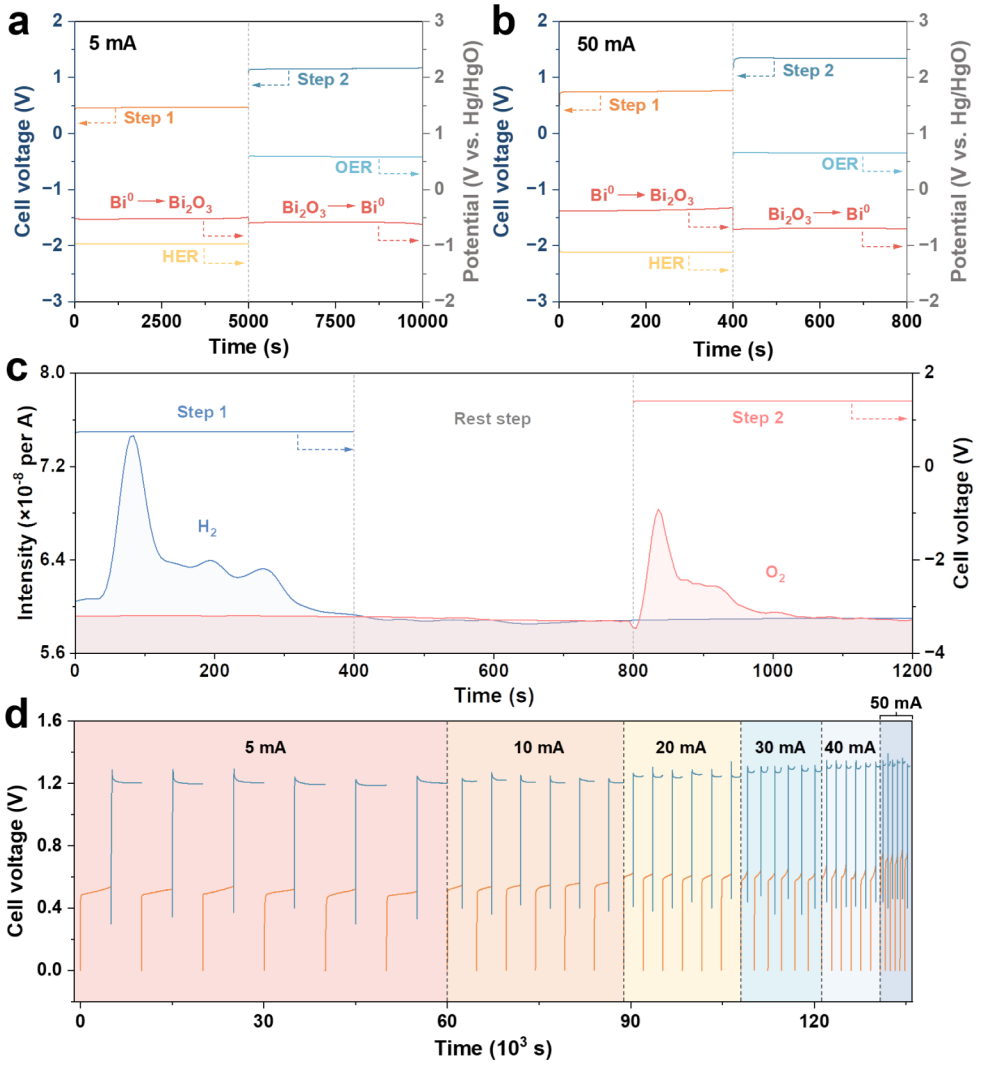

Figure 3. Performance of the decoupled alkaline water electrolysis system. Chronopotentiometry curves (cell voltage versus time) of the cell at a constant current of (a) 5 and (b) 50 mA. The voltages for H_2 production (Step 1) and O_2 production (Step 2) are labeled by orange and blue lines, respectively. Chronopotentiometry data (potential versus time) of the HER electrode (yellow line), the OER electrode (cyan line), and the Bi_2O_3 electrode (red line) are also provided. (c) *In situ* DEMS curves of Step 1 (blue line, H_2 generation) and Step 2 (red line, O_2 generation) in the decoupled water electrolysis process at a constant applied current of 50 mA. (d) Cyclic performance of the separate H_2 and O_2 generation at 5 mA, 10 mA, 20 mA, 30 mA, 40 mA, and 50 mA, where the chronopotentiometry data of Step 1 (H_2 generation) and Step 2 (O_2 generation) are labeled with orange and blue lines, respectively.

Intermediate electrode: $Bi_2O_3 + 3H_2O + 6e^- \rightarrow 2Bi + 6OH^-$ (4)

Overall: $Bi_2O_3 \rightarrow 2Bi + {}^3/_2O_2$ (5)

During the H_2 production process:

Intermediate electrode: $2Bi + 6OH^- \rightarrow Bi_2O_3 + 6e^- + 3H_2O$ (6)

Cathode: $6H_2O + 6e^- \rightarrow 6OH^- + 3H_2$ (7)

Overall: $2Bi + 3H_2O \rightarrow Bi_2O_3 + 3H_2$ (8)

Based on the above discussion, the electrochemical behaviors of synthesized Bi_2O_3 were meticulously investigated using a conventional three-electrode setup in a 1 M KOH electrolyte. Figure 2a displays representative CV curves obtained from the Bi_2O_3 electrode acquired at varying scan rates. A linear correlation between the logarithm (log) of the peak current and the logarithm of the scan rate (Figure 2b) demonstrates that the slopes of the reduction peak (Peak A) and oxidation peak (Peak B) are 0.54 and 0.58, respectively. These findings indicate that the redox processes of Bi_2O_3 are predominantly governed by mass diffusion control (i.e., OH^-) rather than capacitive control.[44]

Furthermore, the rate capability of the Bi_2O_3 electrode was assessed via the GCD test conducted at different current densities (Figure 2c). Notably, the Bi_2O_3 electrode sustains long and flat redox reaction plateaus across a range of current densities, demonstrating excellent reversible capacities of 300.8, 294.6, 289.7, 282.2, 271.3, and 261.7 mA h g^{-1} recorded at rates of 0.2, 0.4, 0.6, 0.8, 1.0, and 2.0 A g^{-1}, respectively (Figure 2d). A comparison of the reversible capacity of Bi_2O_3 with other solid-state redox mediators is provided in Figure S14 and Table S2, wherein Bi_2O_3 evidently outperforms its reported counterparts in terms of capacity. As depicted in Figure 2e, the Bi_2O_3 electrode exhibits commend-

https://doi.org/10.1021/jacsau.4c00710
JACS Au 2024, 4, 3964−3975

able cycling stability and high capacity retention in an alkaline electrolyte at both low and high current densities. Upon reverting the rate to 0.2 A g^{-1}, the discharge capacity of the Bi_2O_3 electrode rebounds to 300.6 mA h g^{-1}, suggesting the remarkable tolerance of the Bi_2O_3 electrode to the high-rate redox reaction. As shown in Figures 2f and S15a, the Bi_2O_3 electrode exhibits an ultraflat discharge plateau and displays long-term recyclability with a 97.1% capacity retention after 100 cycles at 0.2 A g^{-1}. Even with a 10-fold increase in current density to 2.0 A g^{-1}, the Bi_2O_3 electrode still delivers a high capacity of 230.6 mA h g^{-1} with 87.8% capacity retention even after 1000 cycles (Figure 2g and S15b). To further demonstrate the stability of Bi_2O_3/Bi^0 as the redox mediator, Figure S16 illustrates the morphology and atomic ratio of Bi/O of the electrode after 1000 cycles at 2.0 A g^{-1}. The active material remains in the similar nanorod shape in both the reduced (Bi^0) and oxidized (Bi_2O_3) states (Figure S16a_1−a_3 and c_1−c_3), while the size of the nanorods appears larger in the oxidized state. The change in the atomic ratio of Bi/O in Figure S16b,d is consistent with the phase analysis. Table S2 also includes a comparison of the cyclic stability with other solid-state redox mediators, indicating further the feasibility of the Bi_2O_3/Bi^0 redox mediator in a decoupled alkaline water electrolysis system.

Decoupled Alkaline Water Electrolysis Using a Bi_2O_3/Bi^0 ORM

Following electrochemical characterization of the Bi_2O_3 electrode, a membrane-free decoupled alkaline water electrolytic cell was assembled to validate the concept depicted in Scheme 1c. This cell (Figure S17a) comprises a Bi_2O_3 electrode serving as the ORM (2 × 3 cm^2; with a Bi_2O_3 mass loading of 13.6 mg cm^{-2}; Figure S17b), a commercial Pt-coated Ti-mesh electrode for the HER (2 × 3 cm^2; Figure S17c), and a commercial RuO_2/IrO_2-coated Ti-mesh electrode for the OER (2 × 3 cm^2; Figure S17d), which ensure reproducibility and reliability of the experimental results. The performance of the decoupled water electrolysis system, utilizing the Bi_2O_3/Bi^0 ORM in a 1.0 M KOH electrolyte, was investigated by chronopotentiometry measurements. The selected chronopotentiometry curves (cell voltage vs time) for the electrolytic cell, achieved at 5 mA and 50 mA, are presented in Figure 3a,b, and other currents of 10 mA, 20 mA, 30 mA, and 40 mA in Figure S18. It is noted that the corresponding chronopotentiometry data (potential vs time) for both anode and cathode during the electrolysis process were also presented.

In Figure 3a, Step 1, involving H_2 production, exhibits an average cell voltage of ∼0.45 V at 5 mA, arising from the potential difference between the cathodic reduction of H_2O (−0.97 V vs Hg/HgO) and the anodic oxidation of Bi^0 (−0.52 V vs Hg/HgO). Similarly, Step 2, encompassing O_2 production, presents a cell voltage of ∼1.19 V, which is based on the potential difference between the anodic oxidation of OH^- (0.59 V vs Hg/HgO) and the cathodic reduction of Bi_2O_3 (−0.60 V vs Hg/HgO). The Coulombic efficiency of the Bi_2O_3/Bi^0 ORM in decoupled alkaline water electrolysis system can be calculated by comparing the electrolysis time of both steps.[26,45] The electrolysis times for H_2 production (Step 1) and O_2 production (Step 2) are identical (5000 s), suggesting a Coulombic efficiency of approximately 100%.

Figure 3b presents similar results when a higher current of 50 mA was applied to the electrolysis cell. At this current density, the H_2 and O_2 produced in the separate steps were evaluated by *in situ* differential electrochemical mass spectrometry (DEMS). As shown in Figure 3c, the recorded signals indicate that only H_2 was produced in Step 1 by *in situ* DEMS, while O_2 was merely detected in Step 2 following a rest step of 400 s to remove H_2 in the system. Moreover, the drainage method (Figure S19a) was utilized to quantify the H_2/O_2 production with an applied current of 200 mA for 250 s (Figure S20a). Figure S19b,c exhibits that ∼6 mL of H_2 was collected, which is close to the theoretical value (6.34 mL). Using this method, the O_2 volume in Step 2 at 200 mA was measured to be ∼3 mL. Thus, the ratio of H_2 and O_2 is 2:1 in the consecutive cycle of Step 1 and Step 2.

Furthermore, the efficiency of decoupled water electrolysis can be calculated by comparing the total driving voltage (Step 1 + Step 2) with the driving voltage of the corresponding one-step direct water electrolysis, according to the reported works.[15,20] As shown in Figure S20a,b, the efficiency of decoupled alkaline water electrolysis using the Bi_2O_3/Bi^0 ORM is 93% compared with its corresponding one-step direct water electrolysis. In addition, as noted in the introduction section, decoupled alkaline water electrolysis also can use nonprecious electrodes for the H_2/O_2 production.[31,32] In order to verify this, nonprecious electrodes (a Ni foam-based HER electrode and a NiFe-LDH-based OER electrode) were used to further demonstrate the separate H_2 and O_2 production (Figure S21a). Similarly, the efficiency of the decoupled water electrolysis using nonprecious electrodes is 93% compared to the corresponding one-step process (Figure S21b,c).

The stability of H_2 and O_2 generation for decoupled alkaline water electrolysis using the Bi_2O_3/Bi^0 ORM is delineated in Figures 3d and S22. After continuous electrolysis spanning 135,600 s under varying applied currents (5, 10, 20, 30, 40, and 50 mA), the Coulombic efficiency consistently remained at 100%. The polarization in the curves may arise from concentration polarization at the Bi_2O_3/Bi^0 electrode,[46,47] which can be observed by the *in situ* pH test in Figure S23. This result underscores the outstanding stability of the Bi_2O_3-based decoupled device under fluctuating current conditions.

In a decoupled water electrolysis system, the redox mediator plays the key role in balancing the charge transfer. As shown in Figure S24, the Bi_2O_3 electrode can be cycled with different charge depths. Thus, the electrolysis time in each step can be controlled by adjusting the charge depths of the Bi_2O_3 electrode (Figure S25a). Additionally, the electrolysis time in each step can also be controlled by the applied current. The electrolysis times of Step 1 and Step 2 can be increased to 12 h at 2 mA, corresponding to the daytime and nighttime (Figure S25b). Through combining the photovoltaic panel with Bi_2O_3-based decoupled electrolysis cell, a photovoltaic water electrolysis system was constructed to realize the conversion of H_2O and renewable energy to H_2 and O_2 (Figure S26, Movies S1 and S2). Consequently, such properties allow the Bi_2O_3-based decoupled electrolysis system to flexibly utilize renewable energy for H_2 and O_2 production spatially and temporally, such as using solar energy to produce H_2 at the daytime and using wind energy to produce O_2 at the nighttime (Figures S27 and S28).

Exploration to Other Redox Mediators Following ORM Mechanism

Motivated by the insights offered in earlier studies,[35] which underscores the significance of reducible metal oxides in

https://doi.org/10.1021/jacsau.4c00710
JACS Au 2024, 4, 3964−3975

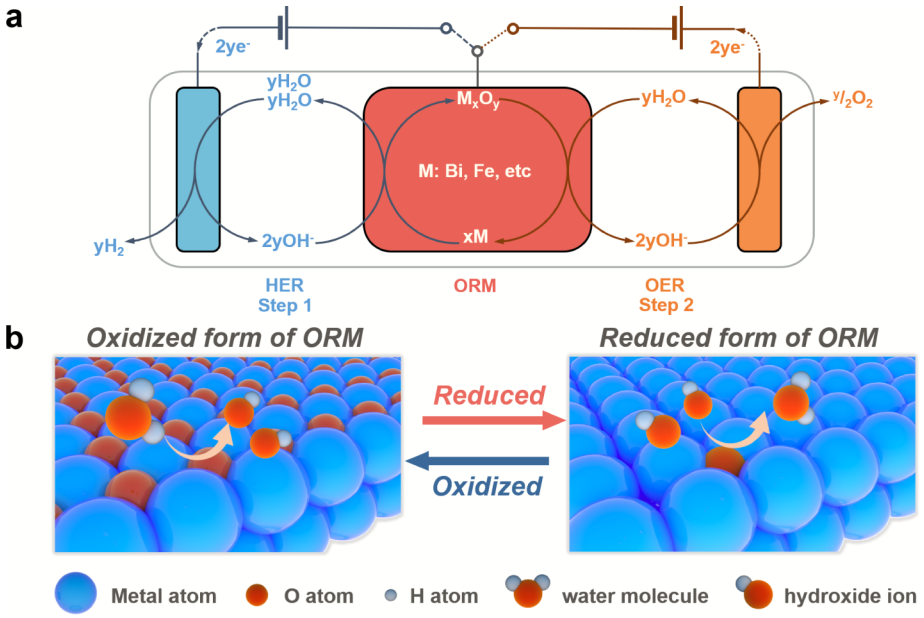

Figure 4. (a) Schematic diagram for decoupled alkaline water electrolysis system based on various reducible metal oxides as the ORMs. (b) Schematic diagram for the redox mechanism of ORMs.

chemical looping processes, it becomes feasible to explore such reducible metal oxides as ORMs in decoupled water splitting. For instance, the redox reactions of Fe_2O_3, commonly used in alkaline batteries, also follow the ORM mechanism. In this study, the Fe_2O_3 nanorods were synthesized through a solvothermal approach (Figure S29). Similarly, the redox couples of Fe_2O_3 are strategically situated between the onset potentials of the HER and the OER (Figure S30a), which signify the reversible redox transformations of $Fe^{3+} \leftrightarrow Fe^{2+} \leftrightarrow Fe^0$ (Figure S30b), in line with the XRD analysis (Figure S31) and prior studies.[48,49] Moreover, the Fe_2O_3 electrode also demonstrates exceptional reversibility and affords a commendable reversible capacity (Figure S32).

It is worth noting that there is still room for improvement in the overall performance of the ORMs in the future. Taking Bi_2O_3/Bi^0 ORM as an example, the slight capacity degradation of the Bi_2O_3 electrode mainly arises from the partial inability of Bi^0 to be reoxidized to Bi_2O_3. Such issue can be resolved by reannealing, enabling the recovered Bi_2O_3 to be reused as an ORM in decoupled water electrolysis system. In addition, functional properties of ORMs hold the potential for further performance enhancement through the incorporation of dopants, carriers, or structural modifications in future research endeavors.

Herein, we propose a mechanistic diagram in Figure 4a for the ORM in the decoupled alkaline water electrolysis system. As an alternative to the ECPB concept, the ORM strategy allows for the redesign of the reaction pathway, breaking down the process into two novel separate subreactions that can occur independently in different spatial or temporal domains. This is achieved by utilizing the redox reactions of ORMs to transport substances and energy within the system. In the HER process, oxygen is extracted from H_2O/OH^- and stored in the ORM through a metal oxidation process. In the OER process, the lattice oxygen of the oxidized ORM is released to complete the water splitting cycle (Figure 4b). With many ORMs readily available and the potential integration with rechargeable alkaline batteries, we believe that the ORMs-based strategy may provide an alternative competitive route for decoupling water splitting.

Integrated System of H_2 Production and Bi_2O_3–Zn Battery

In the context of the decoupled water electrolysis system, the reduction of the oxidized mediator (i.e., $Bi_2O_3 \rightarrow Bi^0$), which is contingent upon the OER in the decoupled system, is crucial for sustained H_2 production. As an alternative approach, this mediator regeneration step is proposed to be supplanted by the discharge step of the Bi_2O_3–Zn battery. It is noted that metallic Zn exhibits superior theoretical capacity (820 mA h g^{-1}) and can be directly adopted as an anode in aqueous electrolytes, which significantly simplifies the battery configuration and assembly.[50] To validate this proposition, the electrochemical performance of the Bi_2O_3–Zn battery was meticulously investigated within a two-electrode configuration. CV curves of the Bi_2O_3–Zn battery, recorded at varying scan rates, are presented in Figure 5a. The linear correlation between the logarithm of the peak current and the logarithm of the scan rate in Figure 5b reveals that the slopes of Peak A and Peak B are 0.59 and 0.54, respectively. These findings align well with the kinetic analysis of the Bi_2O_3 electrode presented in Figure 2b. GCD profiles, along with the corresponding specific capacity data obtained at different current densities for the Bi_2O_3–Zn battery, are furnished in Figure 5c,d. As specific currents increase from 0.2 to 0.4, 0.6, 0.8, 1.0, and 1.5 A g^{-1}, the capacities are consistently maintained at 298.9, 287.3, 278.6, 271.6, 260.5, and 252.4 mA h g^{-1}, respectively. Notably, the Bi_2O_3–Zn battery consistently exhibits stable, flat, and prolonged plateaus during these tests. The rate performance featuring consistent results is depicted in Figure 5e. Noticeably, when the rate shifted back to 0.2 A g^{-1} after the elevated rate performance test, the average discharge capacity of the Bi_2O_3–Zn battery can be largely recovered, indicating superior rate performance. Long-term stability was further assessed at rates of 0.2 A g^{-1} and 1.5 A g^{-1}. At 0.2 A g^{-1} (Figures 5f and S33a), the Bi_2O_3–Zn battery retains a capacity of 206.1 mA h g^{-1} with 70.4% capacity retention after 100 cycles. The long-term cycling performance was also measured at 1.5 A g^{-1} following

https://doi.org/10.1021/jacsau.4c00710
JACS Au 2024, 4, 3964–3975

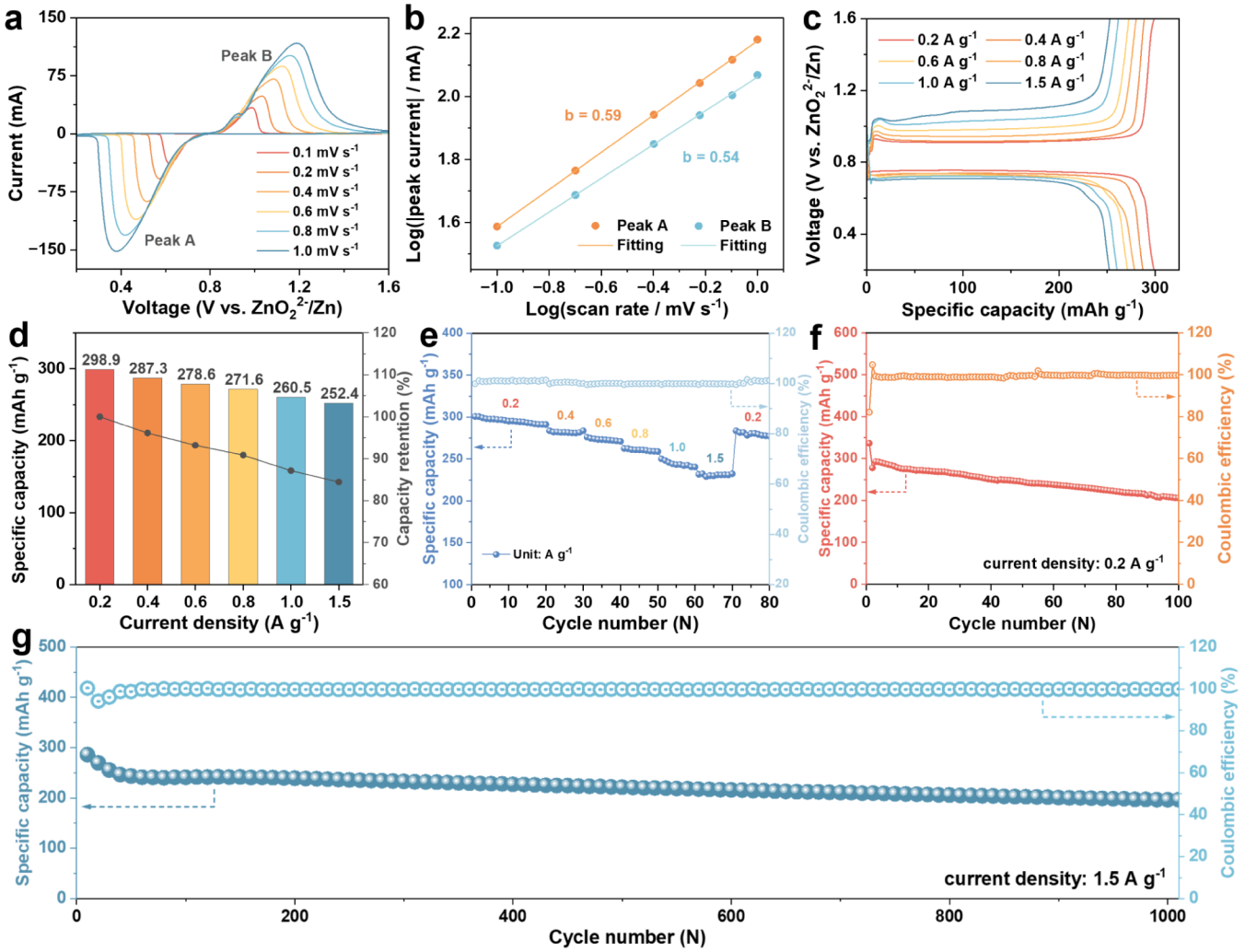

Figure 5. Electrochemical performance of the Bi_2O_3−Zn battery. (a) CV curves at different scan rates. (b) Relationship between the log (peak current) and log (scan rate). (c) GCD curves and (d) corresponding specific capacity at different current densities. (e) Rate performance of the Bi_2O_3−Zn battery. Cycling performance at (f) 0.2 A g^{-1} and (g) 1.5 A g^{-1}.

an initial 10 cycles of activation at 0.2 A g^{-1} (Figure 5g). A significant discharge capacity of 196.4 mA h g^{-1} was maintained with 77.8% capacity retention, even after 1000 cycles. Similar GCD curves at different cycle numbers (Figure S33b) substantiate the stable electrochemical redox reaction process of Bi_2O_3 during extended cycling.

Based on the electrochemical characterizations of the Bi_2O_3−Zn battery, it is viable to substitute the conventional OER process in Step 2 with the discharge process of the Bi_2O_3−Zn battery. This modification is schematically illustrated in Figure 6a, and the intricate operational mechanism can be concisely delineated as follows:

During the discharge process of the Bi_2O_3−Zn battery:

$$\text{Anode: } 3Zn + 12OH^- \rightarrow 3Zn(OH)_4^{2-} + 6e^- \quad (9)$$

$$\text{Cathode: } Bi_2O_3 + 3H_2O + 6e^- \rightarrow 2Bi + 6OH^- \quad (10)$$

$$\text{Overall: } 3Zn + Bi_2O_3 + 3H_2O + 6OH^- \rightarrow 3Zn(OH)_4^{2-} + 2Bi \quad (11)$$

In essence, the configuration presented in Figure 6a offers an intriguing rechargeable cycle that can generate H_2 with concurrent charge of the Bi_2O_3−Zn battery (Step 1) and supply energy upon discharge (Step 2'). The chronopotentiometry curves, representing cell voltage versus time, for this integrated system spanning current densities from 5 to 50 mA, are depicted in Figures 6b,c and S34. Notably, the discharge profile of the Bi_2O_3−Zn battery corresponds well to the H_2 production process, in terms of the running time. Furthermore, the sequential H_2 production step (Step 1) and the discharge step of the Bi_2O_3−Zn battery (Step 2') can be cyclically operated akin to a rechargeable battery for an impressive duration of 135,600 s under diverse applied currents, as illustrated in Figures 6d and S35. In this integration system, the electrolysis of Step 1 to produce H_2 along with the charge of the Bi_2O_3−Zn battery can be driven by renewable energy, while the discharge step (Step 2') of the Bi_2O_3−Zn battery can deliver energy to power electronic devices. As shown in Figure 6e, although the continuous operation of the integration system would consume metallic Zn and increase the concentration of $Zn(OH)_4^{2-}$ in the alkaline electrolyte, metallic Zn can be recovered from the $Zn(OH)_4^{2-}$ alkaline solution through electrolysis. Thanks to the seamless transition between the HER and the Bi_2O_3−Zn battery, this multifunctional integrated system, capable of both power-to-fuel (hydrogen production) and chemical-to-power (rechargeable

https://doi.org/10.1021/jacsau.4c00710
JACS Au 2024, 4, 3964−3975

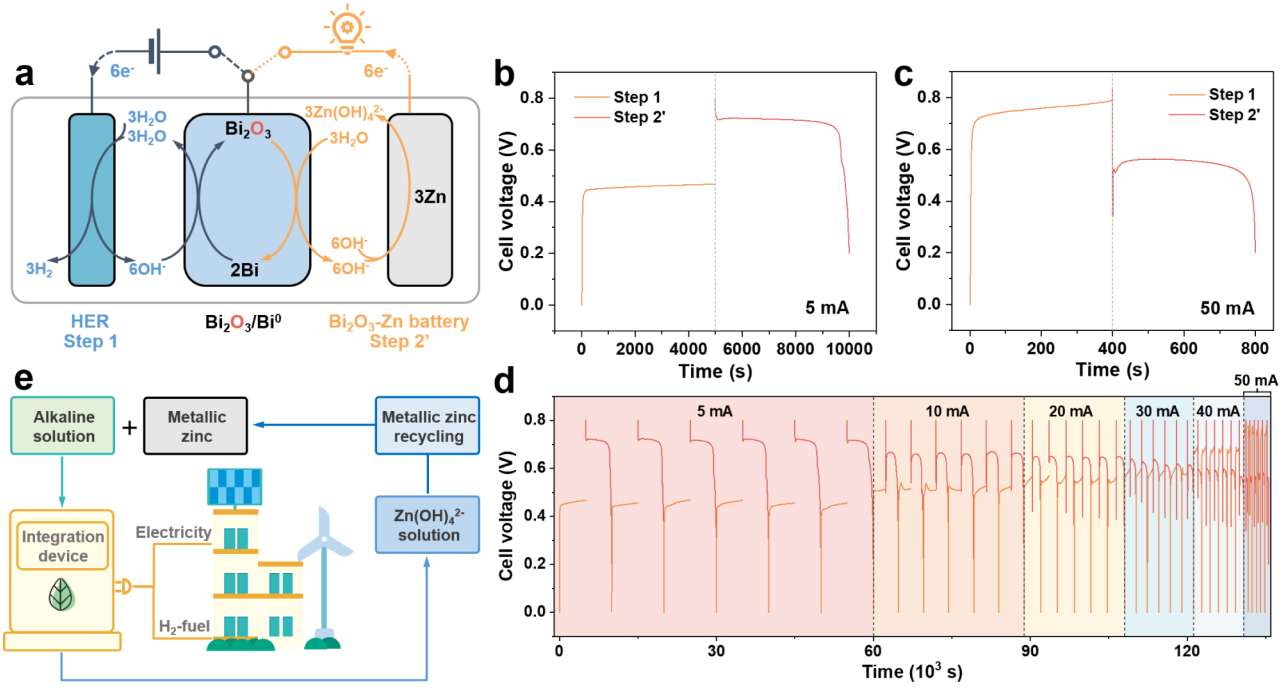

Figure 6. Integration of H_2 production and Bi_2O_3−Zn battery. (a) Schematic diagram for the integrated system of H_2 production and Bi_2O_3−Zn battery. Chronopotentiometry curves (cell voltage versus time) of the H_2 production (Step 1, orange line) and the discharge process of the Bi_2O_3−Zn battery (Step 2′, red line) at a constant current of (b) 5 mA and (c) 50 mA. (d) Cyclic performance of the integrated system at 5 mA, 10 mA, 20 mA, 30 mA, 40 mA, and 50 mA, where the chronopotentiometry data of Step 1 (H_2 generation) and Step 2′ (the discharge process of the Bi_2O_3−Zn battery) are labeled with orange and red lines, respectively. (e) Conceptual illustration of H_2 and electricity production from the integrated system driven by renewable energy.

Bi_2O_3−Zn battery) conversion, demonstrates remarkable flexibility and caters to a wide range of practical applications and demands.

CONCLUSIONS

In conclusion, we have introduced a new concept of ORMs capable of reversibly storing oxygen during the HER and subsequently releasing it to generate oxygen gas under alkaline conditions. This innovation effectively decouples the conventional alkaline electrolysis process into two distinct steps through the oxygen relay, providing an alternative to the ECPB concept in decoupled water splitting systems. In this study, Bi_2O_3/Bi^0 was deliberately chosen as a paradigm of ORMs for its exceptional electrochemical properties, including suitable redox potential, remarkable charge storage capability, and outstanding cycling reversibility and stability in an alkaline electrolyte. Employing a Pt cathode and a RuO_2/IrO_2 anode, we successfully realized decoupled water electrolysis using Bi_2O_3/Bi^0 as the ORM across various current densities. Furthermore, we proposed an integrated system that combines decoupled water electrolysis with a Bi_2O_3−Zn battery, offering a versatile approach to energy transformation and storage. We anticipate that the utilization of ORMs will open new avenues for innovative decoupled electrolyzer design, fostering advancements in future hydrogen technology. Future research following this line is aimed at exploring high-rate ORMs to further enhance the performance of decoupled water electrolysis systems.

MATERIALS AND METHODS

Materials

$Bi(NO_3)_3{\cdot}5H_2O$ (99%), $Ni(NO_3)_3{\cdot}6H_2O$ (99%), $FeSO_4{\cdot}7H_2O$ (99%), $FeCl_3{\cdot}H_2O$ (99%), Na_2SO_4 (99%), ethylene glycol (98%), and acetone (98%) were purchased from Macklin. Ketjen black ECP-600JD (conductive agent), PTFE emulsion (60 wt %), Ni foam (99%), and Ti mesh (100 mesh, 99%) were purchased from CANRD. The commercial Pt-coated Ti-mesh electrode and the commercial RuO_2/IrO_2-coated Ti-mesh electrode were purchased from Baoji Zhiming Special Metal Co., Ltd.

Synthesis of Bi_2O_3

Bi_2O_3 was prepared via a facile hydrothermal route. In detail, $Bi(NO_3)_3{\cdot}5H_2O$ (0.6 g) was added into a mixed solution containing 6 mL of ethylene glycol and 12 mL of acetone and stirred for 45 min. Subsequently, the resulting solution was transferred into a Teflon-lined stainless-steel autoclave and maintained at 160 °C for 6 h. After the reaction, the precipitate was collected and washed with deionized water for several times. Finally, the sample was annealed at 500 °C in the air for 2 h.

Synthesis of Fe_2O_3

Fe_2O_3 was synthesized via a hydrothermal and postannealing process. 0.946 g of $FeCl_3{\cdot}H_2O$ and 0.497 g of Na_2SO_4 were dissolved in a 70 mL solution of deionized water. Subsequently, the resulting solution was transferred into a Teflon-lined stainless-steel autoclave and kept at 160 °C for 6 h. The hydrothermally prepared sample was collected, dried, and further annealed at 600 °C in a flow of Ar for 2 h to obtain Fe_2O_3 nanorods.

Synthesis of NiFe-LDH

The NiFe-LDH OER catalyst was prepared via a facile electrosynthesis method. The Ni foam was used as the working electrode and placed in a typical three-electrode system, by using a Pt plate and saturated calomel electrode (SCE) as the counter and reference electrode, respectively. The electrolyte for the electrosynthesis of

https://doi.org/10.1021/jacsau.4c00710
JACS Au 2024, 4, 3964−3975

NiFe-LDH was obtained by dissolving $Ni(NO_3)_3{\cdot}6H_2O$ (2.18 g) and $FeSO_4{\cdot}7H_2O$ (2.09 g) in 50 mL of deionized water. Chronoamperometry was then carried out at −1.0 V vs SCE for 300 s.

Electrode Preparation

For the high loading mass Bi_2O_3 (or Fe_2O_3) electrode (∼13.6 mg cm^{-2}), the electrode slurry was composed of Bi_2O_3 (or Fe_2O_3), PTFE, and carbon black in a ratio of 8:1:1. The mixture was ground in a mortar for 30 min, and isopropyl alcohol was added to further grind the mixture into a film, which was pressed onto the Ti mesh substrate and dried at 60 °C in a vacuum oven overnight before use.

Materials Characterizations

X-ray diffraction patterns (XRD) were obtained by using a Bruker D8 Phaser with a Cu Kα radiation source (λ = 0.15418 nm). Scanning electron microscopy (SEM, Hitachi S4800, 5 kV) equipped with an energy-dispersive spectrometer was applied to observe the morphologies of Bi_2O_3 and Fe_2O_3. *In situ* Raman spectra were collected on a spectrophotometer (InVia, Renishaw, Germany) by using a 514 nm laser.

Electrochemical Measurements

The electrochemical property of the Bi_2O_3 or Fe_2O_3 electrode was tested by a typical three-electrode system, where the counter electrode is the activated carbon (AC) electrode, and the reference electrode is the Hg/HgO electrode. Cyclic voltammogram (CV) and the linear sweep voltammogram (LSV) were recorded by an electrochemical workstation (CHI 760E). Galvanostatic charge/discharge (GCD) curves were acquired with the same CHI 760E workstation. The cycling performance and rate performance of the single electrode or the Bi_2O_3−Zn battery were validated with a LAND or Neware battery test system.

Gas Detection

An in-line mass spectrometer (MS, INFICON transpector, CPM 3 compact process monitor) was applied to measure the gas evolution of the decoupled water electrolysis process at a constant applied current of 50 mA. The carrier gas (Ar) was supplied at a flow rate of 50 mL min^{-1} to degas the electrolyte and carry out the generated products to MS.

Calculation of Faradaic Efficiency

Faradaic efficiency (*FE*) was calculated by $FE = N_{ex}/N_{th}$, where N_{ex} represents the moles of H_2 or O_2 produced experimentally and N_{th} represents the theoretical moles. N_{ex} was determined using $N_{ex} = V/V_m$, where V is the gas volume measured by the water drainage method and V_m is the molar volume (24.5 L mol^{-1} at RT). N_{th} was calculated using $N_{th} = It/(n \times F)$, where I is the current (200 mA), t is the time (250 s), F is the Faradaic constant (96,500 C mol^{-1}), and n is 2 for H_2 and 4 for O_2.

Decoupled Water Electrolysis Device

The decoupling cell consists of the Bi_2O_3 electrode (2 × 3 cm^2, the mass loading of the Bi_2O_3 is ∼13.6 mg cm^{-2}), the HER electrode (2 × 3 cm^2, commercial Pt-coated Ti-mesh electrode or 2 × 3 cm^2, Ni foam electrode), and the OER electrode (2 × 3 cm^2, commercial RuO_2/IrO_2-coated Ti-mesh electrode or 2 × 3 cm^2, NiFe-LDH electrode). Similarly, the integration system of the H_2 production and the Bi_2O_3−Zn battery was constructed by replacing the previous OER electrode with a zinc electrode (2 × 3 cm^2, 200 μm).

Measurement of Decoupled Water Electrolysis Performance

The electrochemical performance of the above system was investigated by using chronopotentiometry measurements. The process of the electrolysis involves a H_2 production step (i.e., Step 1) and an O_2 production step (i.e., Step 2). In Step 1, the HER electrode and the Bi^0 electrode were acting as the cathode and anode for the H_2 production process. Subsequently, in Step 2, the Bi_2O_3 electrode and the OER electrode were acting as the cathode and anode for the O_2 production process. The cell voltages of Step 1 and Step 2 were used for characterizing the electrolysis profile. The chronopotentiometry data of a single electrode (the Bi_2O_3 electrode, the HER electrode, and the OER electrode) were also detected using a Hg/HgO electrode as a reference electrode during Steps 1 and 2. Tests for the integration system of H_2 production and the Bi_2O_3−Zn battery are analogous to the aforementioned system.

■ ASSOCIATED CONTENT

Supporting Information

The Supporting Information is available free of charge at https://pubs.acs.org/doi/10.1021/jacsau.4c00710.

Additional experimental details, characterizations, electrochemical analyses of the decoupled water electrolysis system using the Bi_2O_3/Bi^0 ORM; schematic diagrams of different water electrolysis systems; results of electrochemical performance of Fe_2O_3-based decoupled water electrolysis system; summary of other solid-state redox mediators reported in literatures (PDF)

Video of photovoltaic decoupled water electrolysis system in HER process (MP4)

Video of photovoltaic decoupled water electrolysis system in OER process (MP4)

■ AUTHOR INFORMATION

Corresponding Author

Zuofeng Chen − *School of Chemical Science and Engineering, Tongji University, Shanghai 200092, China;* orcid.org/0000-0002-2376-2150; Email: zfchen@tongji.edu.cn

Authors

Mingze Xu − *School of Chemical Science and Engineering, Tongji University, Shanghai 200092, China*

Jianying Wang − *School of Chemical Science and Engineering, Tongji University, Shanghai 200092, China*

Shi-Gang Sun − *State Key Lab of Physical Chemistry of Solid Surface, College of Chemistry and Chemical Engineering, Xiamen University, Xiamen 361005, China;* orcid.org/0000-0003-2327-4090

Complete contact information is available at: https://pubs.acs.org/10.1021/jacsau.4c00710

Author Contributions

#M.X. and J.W. contributed equally. CRediT: **Mingze Xu** conceptualization, data curation, formal analysis, investigation, methodology, writing - original draft; **Jianying Wang** conceptualization, investigation, methodology, supervision, validation, writing - review & editing; **Shi-Gang Sun** conceptualization, validation, writing - review & editing; **Zuofeng Chen** conceptualization, funding acquisition, methodology, project administration, resources, supervision, validation, writing - review & editing.

Notes

The authors declare no competing financial interest.

■ ACKNOWLEDGMENTS

This work was supported by the National Natural Science Foundation of China (22072107, 22402150, 21872105), the Natural Science Foundation of Shanghai (23ZR1464800), the Fundamental Research Funds for the Central Universities, and the Science & Technology Commission of Shanghai Municipality (19DZ2271500).

REFERENCES

(1) Dresselhaus, M. S.; Thomas, I. J. N. Alternative energy technologies. *Nature* **2001**, *414*, 332−337.
(2) Turner, J. A. Sustainable hydrogen production. *Science* **2004**, *305*, 972−974.
(3) Chu, S.; Majumdar, A. J. Opportunities and challenges for a sustainable energy future. *Nature* **2012**, *488*, 294−303.
(4) Le Goff, A.; Artero, V.; Jousselme, B.; Tran, P. D.; Guillet, N.; Métayé, R.; Fihri, A.; Palacin, S.; Fontecave, M. J. S. From Hydrogenases to Noble Metal-Free Catalytic Nanomaterials for H_2 Production and Uptake. *Science* **2009**, *326*, 1384−1387.
(5) Orlov, A.; Sillmann, J.; Vigo, I. Better seasonal forecasts for the renewable energy industry. *Nat. Energy* **2020**, *5*, 108−110.
(6) Schill, W.-P. Electricity Storage and the Renewable Energy Transition. *Joule* **2020**, *4*, 2059−2064.
(7) Slobodkin, I.; Davydova, E.; Sananis, M.; Breytus, A.; Rothschild, A. Electrochemical and chemical cycle for high-efficiency decoupled water splitting in a near-neutral electrolyte. *Nat. Mater.* **2024**, *23*, 398−405.
(8) Holladay, J. D.; Hu, J.; King, D. L.; Wang, Y. An overview of hydrogen production technologies. *Catal. Today* **2009**, *139*, 244−260.
(9) Carmo, M.; Fritz, D. L.; Merge, J.; Stolten, D. A comprehensive review on PEM water electrolysis. *Int. J. Hydrog. Energy* **2013**, *38* (12), 4901−4934.
(10) Berger, A.; Segalman, R. A.; Newman, J. Material requirements for membrane separators in a water-splitting photoelectrochemical cell. *Energy Environ. Sci.* **2014**, *7*, 1468−1476.
(11) Liang, S.; Jiang, M.; Luo, H.; Ma, Y.; Yang, J. A High-Rate Electrode with Grotthuss Topochemistry for Membrane-Free Decoupled Acid Water Electrolysis. *Adv. Energy Mater.* **2021**, *11* (40), 2102057.
(12) Mulder, F. M.; Weninger, B. M. H.; Middelkoop, J.; Ooms, F. G. B.; Schreuders, H. Efficient electricity storage with a battolyser, an integrated Ni-Fe battery and electrolyser. *Energy Environ. Sci.* **2017**, *10*, 756−764.
(13) Weninger, B. M. H.; Mulder, F. M. Renewable Hydrogen and Electricity Dispatch with Multiple Ni-Fe Electrode Storage. *ACS Energy Lett.* **2019**, *4*, 567−571.
(14) Ma, Y.; Wu, K.; Long, T.; Yang, J. Solid-State Redox Mediators for Decoupled H_2 Production: Principle and Challenges. *Adv. Energy Mater.* **2023**, *13* (4), 2203455.
(15) Symes, M. D.; Cronin, L. Decoupling hydrogen and oxygen evolution during electrolytic water splitting using an electron-coupled-proton buffer. *Nat. Chem.* **2013**, *5*, 403−409.
(16) Bloor, L. G.; Solarska, R.; Bienkowski, K.; Kulesza, P. J.; Augustynski, J.; Symes, M. D.; Cronin, L. Solar-Driven Water Oxidation and Decoupled Hydrogen Production Mediated by an Electron-Coupled-Proton Buffer. *J. Am. Chem. Soc.* **2016**, *138*, 6707−6710.
(17) Rausch, B.; Symes, M. D.; Chisholm, G.; Cronin, L. Decoupled catalytic hydrogen evolution from a molecular metal oxide redox mediator in water splitting. *Science* **2014**, *345*, 1326−1330.
(18) Rausch, B.; Symes, M. D.; Cronin, L. A Bio-Inspired, Small Molecule Electron-Coupled-Proton Buffer for Decoupling the Half-Reactions of Electrolytic Water Splitting. *J. Am. Chem. Soc.* **2013**, *135*, 13656−13659.
(19) Kirkaldy, N.; Chisholm, G.; Chen, J.-J.; Cronin, L. A practical, organic-mediated, hybrid electrolyser that decouples hydrogen production at high current densities. *Chem. Sci.* **2018**, *9*, 1621−1626.
(20) Chen, L.; Dong, X.; Wang, Y.; Xia, Y. Separating hydrogen and oxygen evolution in alkaline water electrolysis using nickel hydroxide. *Nat. Commun.* **2016**, *7* (1), 11741.
(21) Landman, A.; Dotan, H.; Shter, G. E.; Wullenkord, M.; Houaijia, A.; Maljusch, A.; Grader, G. S.; Rothschild, A. Photoelectrochemical water splitting in separate oxygen and hydrogen cells. *Nat. Mater.* **2017**, *16*, 646−651.
(22) Dotan, H.; Landman, A.; Sheehan, S. W.; Malviya, K. D.; Shter, G. E.; Grave, D. A.; Arzi, Z.; Yehudai, N.; Halabi, M.; Gal, N.; Hadari, N.; Cohen, C.; Rothschild, A.; Grader, G. S. Decoupled hydrogen and oxygen evolution by a two-step electrochemical-chemical cycle for efficient overall water splitting. *Nat. Energy* **2019**, *4*, 786−795.
(23) Ma, Y.; Dong, X.; Wang, Y.; Xia, Y. Decoupling Hydrogen and Oxygen Production in Acidic Water Electrolysis Using a Polytriphenylamine-Based Battery Electrode. *Angew. Chem., Int. Ed.* **2018**, *57*, 2904−2908.
(24) Wang, J.; Ji, L.; Teng, X.; Liu, Y.; Guo, L.; Chen, Z. Decoupling half-reactions of electrolytic water splitting by integrating a polyaniline electrode. *J. Mater. Chem. A* **2019**, *7*, 13149−13153.
(25) Ma, Y.; Guo, Z.; Dong, X.; Wang, Y.; Xia, Y. Organic Proton-Buffer Electrode to Separate Hydrogen and Oxygen Evolution in Acid Water Electrolysis. *Angew. Chem., Int. Ed.* **2019**, *58*, 4622−4626.
(26) Wu, K.; Li, H.; Liang, S.; Ma, Y.; Yang, J. Phenazine-based Compound Realizing Separate Hydrogen and Oxygen Production in Electrolytic Water Splitting. *Angew. Chem., Int. Ed.* **2023**, *135* (23), No. e202303563.
(27) Ma, Z.; Lu, X.; Park, S.; Shinagawa, T.; Okubo, M.; Takanabe, K.; Yamada, A. High-rate Decoupled Water Electrolysis System Integrated with α-MoO_3 as a Redox Mediator with Fast Anhydrous Proton Kinetics. *Adv. Funct. Mater.* **2023**, *33* (25), 2214466.
(28) Landman, A.; Hadash, S.; Shter, G. E.; Ben-Azaria, A.; Dotan, H.; Rothschild, A.; Grader, G. S. High Performance Core/Shell Ni/$Ni(OH)_2$ Electrospun Nanofiber Anodes for Decoupled Water Splitting. *Adv. Funct. Mater.* **2021**, *31* (14), 2008118.
(29) Lv, F.; Qin, Z.; Wu, J.; Pan, L.; Liu, L.; Chen, Y.; Zhao, Y. Decoupled Water Electrolysis Driven by 1 cm^2 Single Perovskite Solar Cell Yielding a Solar-to-Hydrogen Efficiency of 14.4%. *ChemSuschem* **2023**, *16* (1), No. e202201689.
(30) Zheng, X.; Lv, F.; Liu, X.; Zheng, Z.; Chen, Y. Decoupled alkaline water electrolysis by a $K_{0.5}MnO_2$-Ti mediator via K-ion insertion/extraction. *Chem. Commun.* **2023**, *59*, 2138−2141.
(31) Leng, Y.; Chen, G.; Mendoza, A. J.; Tighe, T. B.; Hickner, M. A.; Wang, C.-Y. Solid-State Water Electrolysis with an Alkaline Membrane. *J. Am. Chem. Soc.* **2012**, *134*, 9054−9057.
(32) Zeng, K.; Zhang, D. Recent progress in alkaline water electrolysis for hydrogen production and applications. *Prog. Energy Combust. Sci.* **2010**, *36*, 307−326.
(33) Ormerod, R. M. Solid oxide fuel cells. *Chem. Soc. Rev.* **2003**, *32*, 17−28.
(34) Moçoteguy, P.; Brisse, A. A review and comprehensive analysis of degradation mechanisms of solid oxide electrolysis cells. *Int. J. Hydrog. Energy* **2013**, *38*, 15887−15902.
(35) Zeng, L.; Cheng, Z.; Fan, J. A.; Fan, L. S.; Gong, J. L. Metal oxide redox chemistry for chemical looping processes. *Nat. Rev. Chem.* **2018**, *2*, 349−364.
(36) Zuo, W.; Zhu, W.; Zhao, D.; Sun, Y.; Li, Y.; Liu, J.; Lou, X. W. Bismuth oxide: a versatile high-capacity electrode material for rechargeable aqueous metal-ion batteries. *Energy Environ. Sci.* **2016**, *9*, 2881−2891.
(37) Xu, M.; Niu, Y.; Teng, X.; Gong, S.; Ji, L.; Chen, Z. High-capacity Bi_2O_3 anode for 2.4 V neutral aqueous sodium-ion battery-supercapacitor hybrid device through phase conversion mechanism. *J. Energy Chem.* **2022**, *65*, 605−615.
(38) Xu, M.; Gong, S.; Niu, Y.; Zhang, K.; Liu, T.; Chen, Z. Bismuth-based metal-organic frameworks derived rod-like nanoreactors for neutral aqueous battery-type anode. *Sci. China-Mater.* **2023**, *66*, 106−117.
(39) Choi, B.; Panthi, D.; Nakoji, M.; Kabutomori, T.; Tsutsumi, K.; Tsutsumi, A. A novel water-splitting electrochemical cycle for hydrogen production using an intermediate electrode. *Chem. Eng. Sci.* **2017**, *157*, 200−208.
(40) Torruella, P.; Coll, C.; Martín, G.; López-Conesa, L.; Vila, M.; Díaz-Guerra, C.; Varela, M.; Ruiz-González, M. L.; Piqueras, J.; Peiró, F.; Estradé, S. Assessing Oxygen Vacancies in Bismuth Oxide through EELS Measurements and DFT Simulations. *J. Phys. Chem. C* **2017**, *121*, 24809−24815.
(41) Wang, D.; Zhao, Y.; Liang, G.; Mo, F.; Li, H.; Huang, Z.; Li, X.; Tang, T.; Dong, B.; Zhi, C. A zinc battery with ultra-flat discharge

https://doi.org/10.1021/jacsau.4c00710
JACS Au 2024, 4, 3964−3975

plateau through phase transition mechanism. *Nano Energy* **2020**, *71*, 104583.
(42) Yao, D.; Tang, C.; Li, L.; Xia, B.; Vasileff, A.; Jin, H.; Zhang, Y.; Qiao, S.-Z. In Situ Fragmented Bismuth Nanoparticles for Electrocatalytic Nitrogen Reduction. *Adv. Energy Mater.* **2020**, *10* (33), 2001289.
(43) Jia, G.; Wang, Y.; Sun, M.; Zhang, H.; Li, L.; Shi, Y.; Zhang, L.; Cui, X.; Lo, T. W. B.; Huang, B.; Yu, J. C. Size Effects of Highly Dispersed Bismuth Nanoparticles on Electrocatalytic Reduction of Carbon Dioxide to Formic Acid. *J. Am. Chem. Soc.* **2023**, *145*, 14133−14142.
(44) Augustyn, V.; Come, J.; Lowe, M. A.; Kim, J. W.; Taberna, P.-L.; Tolbert, S. H.; Abruña, H. D.; Simon, P.; Dunn, B. High-rate electrochemical energy storage through Li^+ intercalation pseudocapacitance. *Nat. Mater.* **2013**, *12*, 518−522.
(45) Xiao, J.; Li, Q.; Bi, Y.; Cai, M.; Dunn, B.; Glossmann, T.; Liu, J.; Osaka, T.; Sugiura, R.; Wu, B.; Yang, J.; Zhang, J.-G.; Whittingham, M. S. Understanding and applying coulombic efficiency in lithium metal batteries. *Nat. Energy* **2020**, *5*, 561−568.
(46) Wu, J. Understanding the Electric Double-Layer Structure, Capacitance, and Charging Dynamics. *Chem. Rev.* **2022**, *122*, 10821−10859.
(47) Guo, Y.; Li, X.; Guo, H.; Qin, Q.; Wang, Z.; Wang, J.; Yan, G. Visualization of concentration polarization in thick electrodes. *Energy Storage Mater.* **2022**, *51*, 476−485.
(48) Wang, H.; Liang, Y.; Gong, M.; Li, Y.; Chang, W.; Mefford, T.; Zhou, J.; Wang, J.; Regier, T.; Wei, F.; Dai, H. An ultrafast nickel−iron battery from strongly coupled inorganic nanoparticle/nanocarbon hybrid materials. *Nat. Commun.* **2012**, *3* (1), 917.
(49) Li, R.; Wang, Y.; Zhou, C.; Wang, C.; Ba, X.; Li, Y.; Huang, X.; Liu, J. Carbon-Stabilized High-Capacity Ferroferric Oxide Nanorod Array for Flexible Solid-State Alkaline Battery-Supercapacitor Hybrid Device with High Environmental Suitability. *Adv. Funct. Mater.* **2015**, *25*, 5384−5394.
(50) Hao, J.; Li, X.; Zeng, X.; Li, D.; Mao, J.; Guo, Z. Deeply understanding the Zn anode behaviour and corresponding improvement strategies in different aqueous Zn-based batteries. *Energy Environ. Sci.* **2020**, *13*, 3917−3949.

https://doi.org/10.1021/jacsau.4c00710
JACS Au 2024, 4, 3964−3975